ACS APPLIED MATERIALS & INTERFACES

Research Article

www.acsami.org

MoS_2 Nanocube Structures as Catalysts for Electrochemical H_2 Evolution from Acidic Aqueous Solutions

A. Wouter Maijenburg,[†,‡] Morrisa Regis,[‡,∥] Azusa N. Hattori,[§] Hidekazu Tanaka,[§] Kyoung-Shin Choi,[‡,∥] and Johan E. ten Elshof*[,†]

[†]Inorganic Materials Science, MESA+ Institute for Nanotechnology, University of Twente, P.O. Box 217, 7500 AE Enschede, The Netherlands

[‡]Department of Chemistry, Purdue University, 560 Oval Drive, West Lafayette, Indiana 47907-2084, United States

[§]Institute of Scientific and Industrial Research, Osaka University, 8-1 Mihogaoka, Ibaraki, Osaka 567-0047, Japan

ABSTRACT: Core−shell PMMA−Au nanocube structures made by a combination of nanoimprint lithography and sidewall deposition were used as template for electrodeposition of MoS_2, Ni, and Pt. Linear sweep voltammetry experiments obtained in an aqueous solution containing 0.29 M H_2SO_4 (pH 0.24) showed that the onset potential of the core−shell−shell PMMA−Au−MoS_2 nanocube electrode for the hydrogen evolution reaction (HER) was shifted to the positive direction (i.e., requiring a lower overpotential) by 20−40 mV compared to planar MoS_2 films. This indicates that the nanocube electrodes have a significantly increased HER activity, which is probably because of a higher density of catalytically active edge sites available at the nanocube surface. It was also found that the HER activity initially increased with increasing MoS_2 deposition time, but decreased after deposition for 60 min because the edges of the nanocubes became rounded, thereby decreasing the number of active edge sites. By depositing Ni and Pt on top of PMMA−Au nanocubes, it was shown that this method can also be used for the synthesis of nanocube structures with varying compositions.

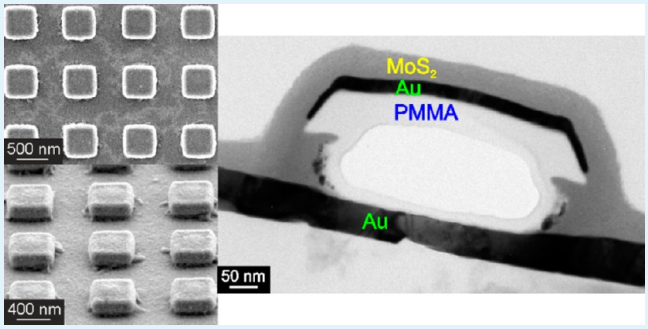

KEYWORDS: *molybdenum disulfide, electrochemical deposition, catalyst, nanocubes, nanoboxes, water splitting*

INTRODUCTION

Photocatalytic or photoelectrochemical water splitting is emerging as a promising clean technique for the synthesis of H_2 gas, which could be used as a clean and renewable energy source. The main active component of most photocatalysts and photoelectrodes is an inorganic semiconductor with appropriate band edge positions for water splitting and a suitable band gap (ca. 2 eV) to utilize visible light. One of the major sources for efficiency loss in these systems is surface recombination of charge carriers caused by a poorly active catalytic surface of the semiconductor for the H_2 or O_2 evolution reactions (HER and OER, respectively). Efficiency loss can be significantly reduced by addition of a catalyst for the HER or OER.[1−3] For the HER, Pt is the most efficient cocatalyst, but large-scale application of Pt or Pt-based composites or alloys is impossible due to its high cost and low abundance. Therefore, it is advantageous to investigate other types of materials that can mimic the performance of Pt for the HER.[4−6]

An interesting material to use as a HER catalyst is MoS_2, because of its high chemical stability in, for example, strong acids.[7] In industry, MoS_2 is a well-known catalyst for hydrodesulfurization of petroleum.[8−10] Furthermore, MoS_2 is used as a solid lubricant[11−13] and in photo-oxidation of organics.[14] MoS_2 is a layered chalcogenide with sheets of S−Mo−S layers, thus exposing Mo $(10\underline{1}0)$ edges, S $(\underline{1}010)$ edges, and basal planes.[15,16] Since the first report of MoS_2 as HER catalyst by Sobczynski,[7] several studies have shown that the edge sites of MoS_2 are catalytically the most active sites for H_2 evolution.[6,15,17,18] Most research is therefore focused on nanostructuring MoS_2 to increase its efficiency for the HER by creating a higher concentration of active edge sites and thereby decreasing the required overpotential.[4,7,17−21] To date, several MoS_2 nanostructures were published that showed an excellent HER performance compared to planar films. Among these are crystalline, single-layered MoS_2 polygons,[17] amorphous MoS_3 films made by electrodeposition,[5,22] double-gyroid porous MoS_2 nanostructures[19] and core−shell MoO_3−MoS_2 nanowires.[4]

The most common method for MoS_2 deposition is a thermal deposition process employing high temperature, high pressure and the use of toxic H_2S gas as one of the precursors.[7,17,18] Although these processes are widely used in industry, safer and less expensive processes are preferred. One of these processes is

Received: November 12, 2013
Accepted: January 20, 2014
Published: January 20, 2014

   dx.doi.org/10.1021/am405075f | ACS Appl. Mater. Interfaces 2014, 6, 2003−2010

electrochemical deposition of amorphous MoS_3 films, which are thought to be reduced to MoS_2 under the experimental conditions of H_2 evolution.[5,22] Another low-cost and scalable process is in situ photoassisted deposition of MoS_2 on top of a semiconductor with proper band edge positions, for example, $Zn_xCd_{1-x}S$, for improved H_2 evolution rates.[23]

In this study, core−shell−shell PMMA−Au−MoS_2 nanocube structures (abbreviated to MoS_2 nanocube structures) were prepared by electrodeposition of MoS_2 on PMMA−Au nanocube structures. These PMMA−Au nanocube structures were made by a combination of nanoimprint lithography (NIL) and sidewall deposition as schematically shown in Figure 1.

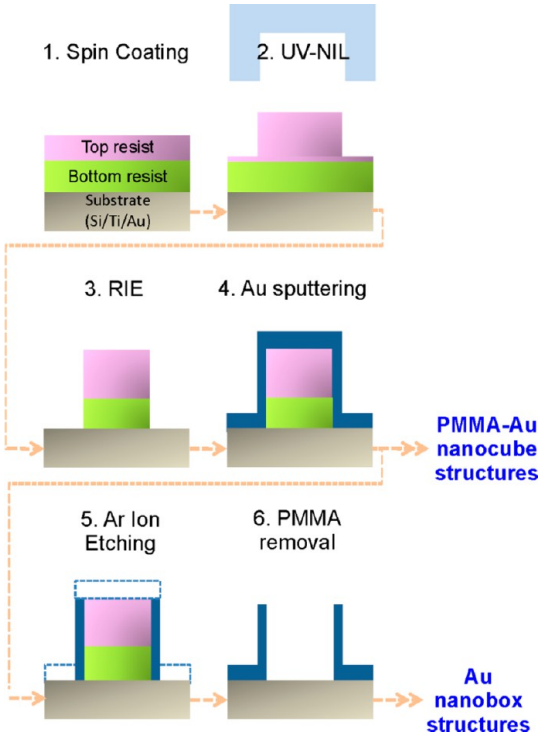

Figure 1. Schematic representation of UV-NIL process used for the preparation of PMMA−Au nanocubes and Au nanoboxes: Spin-coating of resist layers (step 1), ultraviolet nanoimprint lithography (UV-NIL) (step 2), reactive ion etching (RIE) of residual resist layers (step 3), Au sputtering for the formation of PMMA-Au nanocube structures (step 4), selective Ar ion etching of unwanted Au layer from the top (step 5), and PMMA removal using acetone for the formation of Au nanobox structures (step 6).

NIL is a promising technique to create structures with innovative shapes, since NIL can reproducibly create patterns with resolutions down to 10 nm over a large substrate area at high throughput and low cost.[24−28] Subsequent sidewall deposition of, for example, Au, ZnO, or Mo on the sides and top of the resist used for NIL has proven its feasibility for making 3D hollow nanobox structures with dimensions below the dimensions of the mold, and these structures were also used in optoelectronic devices.[26−28] PMMA-Au nanocube structures also provide a perfect and reproducible substrate for making nanocube structures containing any desired material by electrodeposition. In this study, MoS_2 nanocube structures were prepared by electrodeposition using patterned PMMA−Au nanocube arrays as the substrates. Nanocube arrays with cubes having lateral dimensions of 200 or 500 nm were prepared. The resulting MoS_2 nanostructures were expected to contain an increased density of catalytically active edge sites for the HER. Their electrocatalytic activities were therefore compared with the activity of planar MoS_2 films prepared under the same electrodeposition conditions. Here, we report the synthesis and HER properties of these MoS_2 nanocube electrodes.

EXPERIMENTAL DETAILS

Resist polymers NX-2030 and NX-3032 were purchased from Nanonex; ammonium tetrathiomolybdate ($(NH_4)_2MoS_4$, purity 99.98%), potassium chloride (KCl, purity 99.999%), ammonium chloride (NH_4Cl, purity 99.5%), and sulfuric acid (H_2SO_4, 96% in water) were purchased from Acros Organics; formamide (purity 99.5+%) and chloroplatinic acid hexahydrate ($H_2PtCl_6{\cdot}6H_2O$, powder and chunks) were purchased from Sigma-Aldrich; and nickel sulfate hexahydrate ($NiSO_4{\cdot}6H_2O$, purity 99%) and boric acid (H_3BO_3, purity 99.99%) were purchased from Merck. Milli-Q water with a resistivity of 18.2 MΩ·cm was used in all experiments.

The UV (ultraviolet)-NIL process used for the formation of the nanocube structures was slightly modified with respect to the previously published procedure.[27] In short, a bilayer organic resist system consisting of a bottom layer of thermally curable resin (NX-2030) and a top layer of UV-curable resin (NX-3032) was employed. The UV-NIL process was performed by a nanoimprinter (Eitre 3, Obducat) at a pressure of 30 mbar at room temperature with 1 min of UV exposure. Using a reactive ion etching (RIE) system (RIE-10NR, Samco), the top and bottom residual layers were removed by a CF_4 and O_2 plasma process, respectively. A 10−20 nm thick Au layer was deposited at room temperature for 120 s at 8 mL of Ar flow (STP) using an RF sputter system (SC701HMC, Sanyu, Japan), which was operated at 500 W input power. For the formation of nanobox structures, an additional ion etching process (EIS-200ER, Elionix, Japan) with Ar was applied as an anisotropic etching process after deposition, which etched away the top Au layer from the nanocube structures. Figure 1 gives a schematic representation of this process.

MoS_2, Pt, and Ni were deposited on Au nanocube or nanobox structures and flat Au films by electrodeposition in a three-electrode setup. Here, the substrate was the working electrode, and a Pt sheet and Ag/AgCl in 3 M KCl (Metrohm Autolab) were used as counter and reference electrode, respectively. These electrodes were connected to an Autolab PGSTAT 128N potentiostat. MoS_2 was electrodeposited from a formamide solution containing 0.002 M $(NH_4)_2MoS_4$, 0.04 M KCl, and 0.2 M NH_4Cl at a potential of −0.6 V vs Ag/AgCl. After deposition, MoS_2 was annealed under a constant flow of Ar gas for 1 h at 400 °C. Ni was deposited from an aqueous electrolyte solution containing 0.23 M $NiSO_4{\cdot}6H_2O$ and 0.15 M H_3BO_3 at a potential of −1.0 V vs Ag/AgCl. Pt was deposited using an aqueous electrolyte solution containing 0.01 M $H_2PtCl_6{\cdot}6H_2O$ at a potential of −0.3 V vs Ag/AgCl.

Scanning electron microscopy (SEM) images were taken with a Zeiss Merlin HRSEM instrument. Transmission electron microscopy (TEM) images were taken with an Analytical TEM apparatus from FEI Instruments. Electrochemical characterization was performed by linear sweep voltammetry (LSV) using the same three-electrode setup as used for electrodeposition, but using a glassy carbon rod (7 mm diameter, 50 mm length, Alfa Aesar) as counter electrode. The electrolyte was an aqueous solution containing 0.29 M H_2SO_4 (pH 0.24), which was purged with N_2 gas for at least 30 min prior to the LSV measurements in order to remove any dissolved O_2. LSV curves were measured twice for every sample in the negative direction from 0.07 to −0.8 V vs Ag/AgCl using a step potential of −0.3 mV and a scan rate of 5 mV/s. Prior and after the LSV measurements, a constant potential of −0.4 V vs Ag/AgCl was applied for 10 min to reduce any oxidized material and verification of the system's chemical stability. The solution was stirred during all measurements. The potential was converted to the RHE reference electrode by

$$E\ (\text{vs RHE}) = E\ (\text{vs Ag/AgCl}) + E_{\text{Ag/AgCl}}\ (\text{ref}) + 0.0591\ \text{V}{\cdot}\text{pH} \quad (1)$$

dx.doi.org/10.1021/am405075f | ACS Appl. Mater. Interfaces 2014, 6, 2003−2010

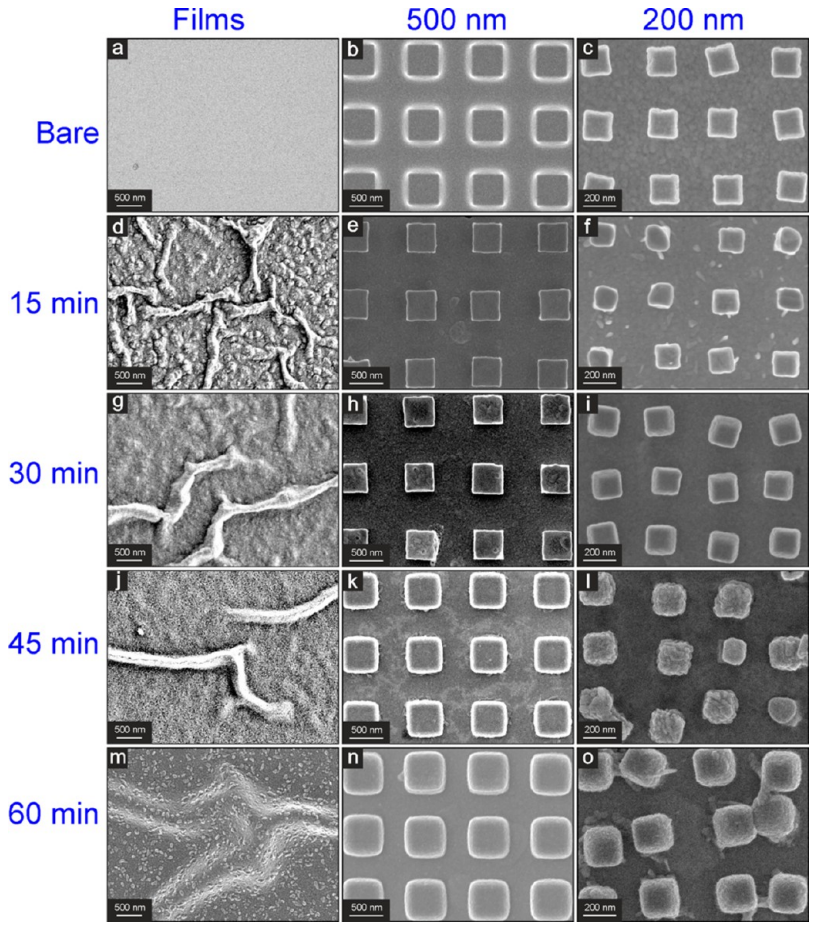

Figure 2. SEM images of electrodeposited MoS_2 films and nanocube structures: (a) bare Au substrate, (b) Au nanocube structures, lateral size ~ 500 nm, (c) Au nanocube structures, lateral size ~ 200 nm, (d) MoS_2 film after 15 min MoS_2 deposition, (e) MoS_2 nanocube structures, lateral size ~ 500 nm, 15 min MoS_2 deposition, (f) MoS_2 nanocube structures, lateral size ~ 200 nm, 15 min MoS_2 deposition, (g) MoS_2 film, 30 min MoS_2 deposition, (h) MoS_2 nanocube structures, lateral size ~ 500 nm, 30 min MoS_2 deposition, (i) MoS_2 nanocube structures, lateral size ~ 200 nm, 30 min MoS_2 deposition, (j) MoS_2 film, 45 min MoS_2 deposition, (k) MoS_2 nanocube structures, lateral size ~ 500 nm, 45 min MoS_2 deposition, (l) MoS_2 nanocube structures, lateral size ~ 200 nm, 45 min MoS_2 deposition, (m) MoS_2 film, 60 min MoS_2 deposition, (n) MoS_2 nanocube structures, lateral size ~ 500 nm, 60 min MoS_2 deposition, (o) MoS_2 nanocube structures, lateral size ~ 200 nm, 60 min MoS_2 deposition.

$$E_{Ag/AgCl}\,(\text{ref}) = 0.1976\ \text{V vs RHE at 25 °C} \quad (2)$$

RESULTS AND DISCUSSION

Figure 2 shows SEM images of MoS_2 films and PMMA–Au–MoS_2 nanocube structures after electrodeposition and annealing. From the SEM images in the left column, it can be concluded that the MoS_2 films were not completely smooth, since wrinkles were observed of similar dimensions as the nanocube structures. More interestingly, no wrinkles were observed on or in between the nanocube structures and the PMMA–Au nanocube structures were smoothly covered with MoS_2. Comparison with a MoS_2 film before annealing (Figure 3) showed that these wrinkles were formed during thermal annealing by compressive stress. As shown by Hendricks and Lee, this stress can be released by incorporation of a nanostructure or nanoparticles in a polyelectrolyte multilayer coating on PDMS, thereby preventing wrinkle formation.[29] Since the wrinkles observed on the MoS_2 films have similar dimensions as the nanocubes used in this study, it is expected that the deposition of MoS_2 on discrete nanocube structures prevented the build-up of compressive stress and therefore the formation of wrinkles on the nanocubes.

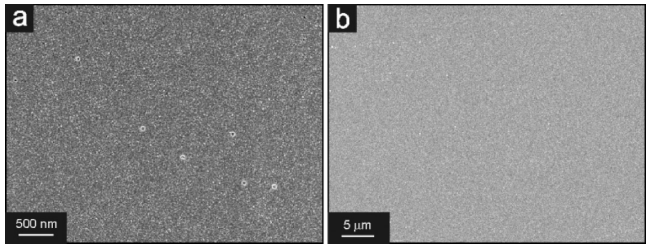

Figure 3. (a) HR-SEM and (b) SEM images of as-deposited MoS_2 film after 45 min MoS_2 deposition.

For the nanocube structures, a small decrease in nanocube size was observed for short deposition times (Figure 2e,f), but, upon prolonged deposition, the thickness of the MoS_2 layer gradually increased with deposition time at an average deposition rate of ~40 nm/h. The reason for the initial decrease in nanocube size is that formamide, which is the solvent used for MoS_2 deposition, was able to penetrate the Au layer on top of the PMMA nanocube structures and dissolved part of the polymeric resist underneath this Au layer. The flexibility of the Au layer caused the core–shell nanocube structure to partly collapse. Since smaller nanocubes with a larger relative surface area have a higher surface energy per unit

dx.doi.org/10.1021/am405075f | ACS Appl. Mater. Interfaces 2014, 6, 2003–2010

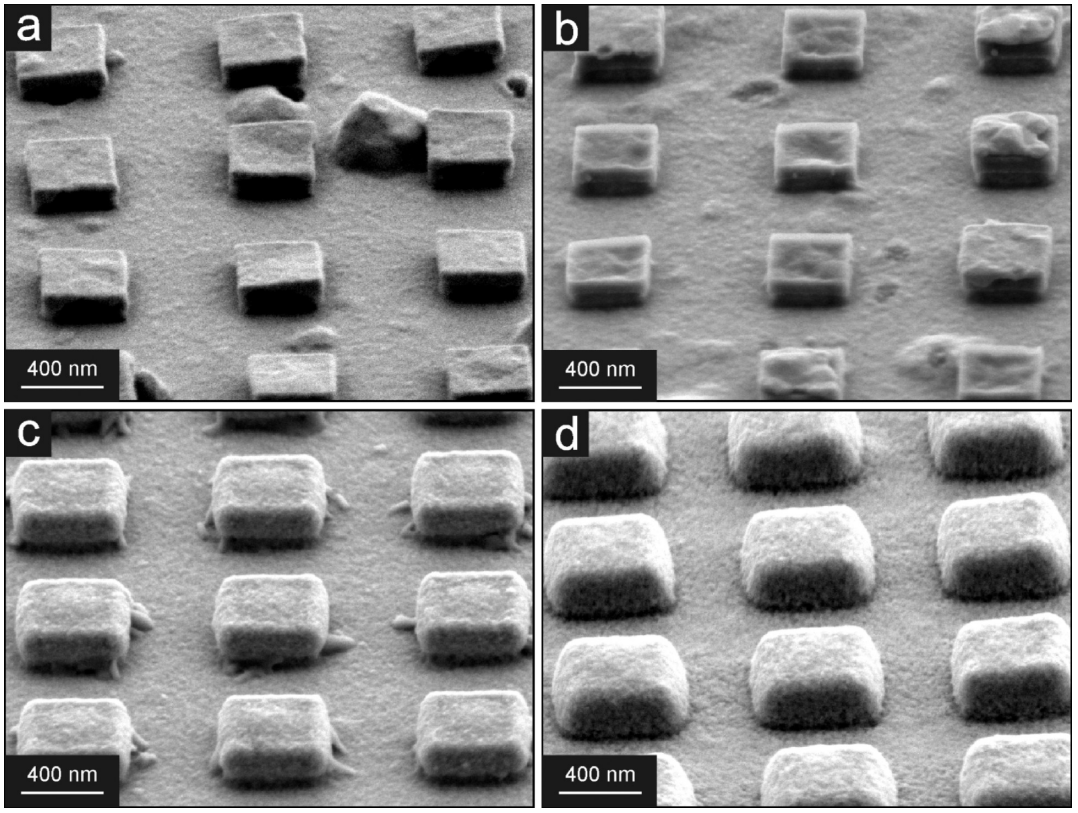

Figure 4. Side-view SEM images of MoS_2 nanocube structures with a lateral size of approximately 500 nm after electrodeposition for (a) 15 min, (b) 30 min, (c) 45 min, and (d) 60 min.

volume, the shape of the nanocube structures with lateral dimensions of 200 nm may be more susceptible to deformation by formamide etching.

Another interesting observation was that, after 30 min of MoS_2 deposition, the sharp edges of the nanocube structures were still clearly visible (Figures 2h,i and 4a,b), but after 45 min they became more rounded (Figures 2k,l and 4c,d). The reason can be found in the layered structure of MoS_2, in which it is energetically more favorable to expose fewer edge sites and form a continuous blanket on top of the nanocube structures. Since smaller nanocubes with a larger relative surface area have a higher surface energy per unit volume, the smaller structures with lateral dimensions of 200 nm obtained a more rounded shape than the larger nanocube structures with lateral dimensions of 500 nm.

In Figure 5, a TEM image of a cross section of a MoS_2 nanocube structure with a lateral size of ~500 nm after electrodeposition for 60 min is shown. Figure 5a shows the different phases present in a single nanocube on a Au substrate, where the PMMA core was partly dissolved during sample preparation for TEM imaging. On top of the PMMA core, a 10−20 nm thick Au layer and a ~40 nm thick MoS_2 layer were visible. Figure 5b is a high resolution TEM image at the top left corner of a MoS_2 nanocube structure showing the arrangement of individual MoS_2 layers at the atomic level. It was found that MoS_2 layers are composed of numerous nanoscale MoS_2 domains which are randomly oriented to each other, but with a strong preferential orientation of (002) planes parallel to the underlying Au substrate as confirmed by fast Fourier transform (FFT) analysis (Figure 5c−j). The diffuse ring in the FFT patterns represents the reciprocal distance between two adjacent MoS_2 planes in the [002] direction. Also displayed in the FFT patterns is a numerical value r for the degree of orientational (an)isotropy within the ring. It is defined as $r = I_{min}/I_{max}$, where I_{max} is the intensity at its maximum value along the (002) ring, that is, the direction in which the MoS_2 planes show the highest degree of organization, and the intensity I_{min} is measured in the direction perpendicular to that. At the sidewall and on top of a nanocube structure, MoS_2 growth was able to proceed parallel to the underlying Au interface. This is illustrated by the identical FFT patterns in Figure 5c,d and e,f, respectively, in which the r value shows that the MoS_2 planes are oriented parallel to the underlying Au layer. The only difference between bottom and top of the MoS_2 layer in these areas is a slight increase in r value, ranging from $r \sim 0.83 \pm 0.02$ near the Au interface to $r \sim 0.87 \pm 0.02$ at the top surface. Many other areas were also analyzed, and they provided average r values of 0.83 ± 0.01 and 0.88 ± 0.04 near the Au surface and top of the MoS_2 layer, respectively. On the other hand, the MoS_2 layers from the top surface and sidewalls meet at the corner of a nanocube structure, so that organization is expected to become more irregular in that area. This process is visible when looking at the FFT patterns made from bottom to top of the MoS_2 layer at the edge of a nanocube (Figure 5g−j). At the bottom of the MoS_2 layer, a sharp transition from MoS_2 planes arranged parallel to the side wall of the nanocube (Figure 5g) to MoS_2 planes arranged parallel to the top surface of the nanocube (Figure 5h) can be observed. When analyzing the FFT patterns of areas closer to the top of the MoS_2 layer (Figure 5i,j), it can be observed that the alignment of the MoS_2 planes decreased accordingly, with a maximum r value of 0.93 ± 0.02 at the top corner of the MoS_2 nanocube. The decrease in degree of order can be explained by curvature of the MoS_2 layers by the blanketing effect, as can be observed in Figures 2

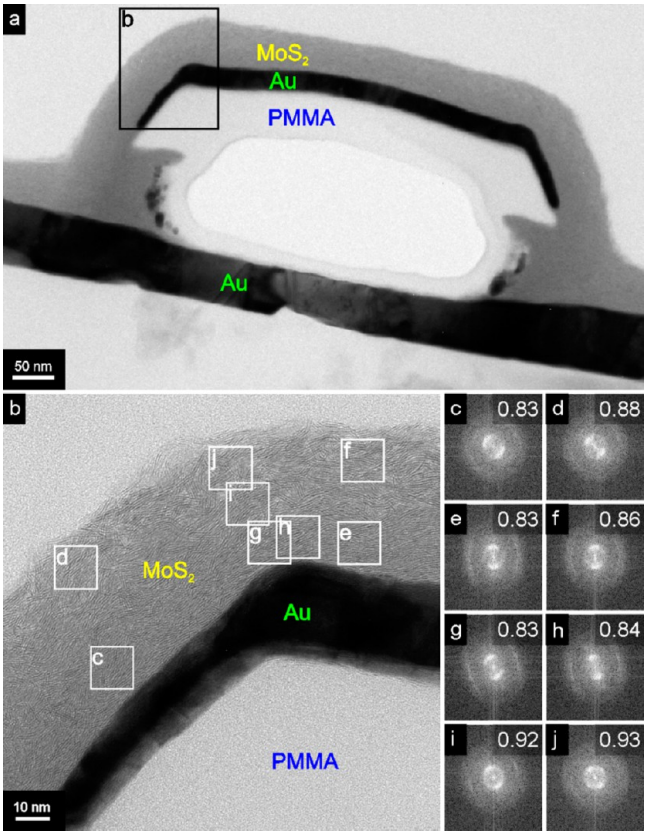

Figure 5. (a) TEM image of a MoS_2 nanocube structure with a lateral size of approximately 500 nm after electrodeposition for 60 min, (b) HR-TEM image of the area indicated in (a), and (c–j) fast Fourier transform (FFT) images of the respective areas as indicated in (b). The numbers in the upper right corners of (c–j) are the *r* values, which express the degree of organizational anisotropy in the respective areas.

and 4. Since several studies showed that the edge sites of MoS_2 planes are catalytically the most active sites for H_2 evolution,[6,15,17,18] it is expected a priori that the regions near the corners of a MoS_2 nanocube before the blanketing effect are catalytically more active for hydrogen evolution than the planar regions.

Figure 6 shows LSV curves and the corresponding Tafel plots measured on different MoS_2 samples. In Figure 6a–c, MoS_2 was deposited on a Au film, 500 nm nanocube structures and 200 nm nanocube structures, respectively. On all MoS_2 (nano)structures, the onset potential for H_2 evolution shifted to more positive potentials (i.e., less overpotential) when the deposition time increased from 15 to 45 min, which is an indication for increasing activity toward H_2 formation, but it shifted back to more negative potentials when the deposition time was increased to 60 min. This may be related to a decreased conductivity of thicker MoS_2 layers, but for the nanocube structures this may also be explained by the formation of rounded edges after 45–60 min deposition, in which the number of catalytically active edge sites of the disordered MoS_2 layers decreased by the "blanket" formed over the nanocube structures, as shown in Figures 2k,l,n,o and 4c,d. The high activity of the MoS_2 film deposited for 45 min can be explained by cracking of the wrinkles (Figure 2j), which exposed the edge sites within these wrinkles. As such cracks were smoothly covered with MoS_2 after deposition for 60 min (Figure 2m), apparently the HER activity decreased upon prolonged deposition.

In Figure 6d, all MoS_2 structures after deposition for 45 min were compared with each other, and with a Au film without MoS_2. It can be seen that the onset potential for H_2 formation is more positive for both MoS_2 nanocube structures than for the MoS_2 film, which implies a higher H_2 evolution activity. The presented current densities are calculated based on the real surface area, therefore surface area differences between flat and structured films are not the cause for the observed differences in the onset potential or Tafel slope. Even though the observed wrinkles on the MoS_2 films have similar dimensions as the nanocube structures, these wrinkles do not expose a higher concentration of edge sites compared to the nanocube structures, which probably explains the observed later onset potential of the MoS_2 films. The smaller nanocube structures show a slightly earlier onset potential than the larger nanostructures, which is in agreement with the larger number of edge sites per unit surface area.

During the H_2 formation experiments, the stability of the MoS_2 structures under these strongly acidic conditions was evaluated by recording two LSV curves per sample, which resulted in comparable current densities. Before and after both LSV curves were recorded, a potentiostatic measurement was performed at −0.4 V vs Ag/AgCl for 10 min, which also indicated that the performance of these MoS_2 structures remained the same before and after LSV measurements. We repeated the same measurements again after storage of one of the samples for 8 months (500 nm nanocubes after 45 min MoS_2 deposition), which confirmed the stability of the MoS_2 structures. Preliminary results even indicated an increase in activity toward the H_2 evolution reaction compared to the measurements performed on fresh samples. SEM analysis did not indicate any sign of deterioration of the MoS_2 structures after H_2 evolution experiments under acidic conditions.

Table 1 gives an overview of all relevant data that were extracted from the LSV measurements and Tafel plots in Figure 6. The Tafel slope of a given material can be used to distinguish between different mechanistic pathways involving the three reactions generally involved in H_2 evolution, that is, Volmer, Tafel, and Heyrovsky steps:

Volmer:

$$H^+ + e^- \rightarrow H_{ads} \quad (3)$$

Tafel:

$$H_{ads} + H_{ads} \rightarrow H_2 \quad (4)$$

Heyrovsky:

$$H_{ads} + H^+ + e^- \rightarrow H_2 \quad (5)$$

If the first reaction step (Volmer or discharge reaction) is rate-determining, a Tafel slope of 118 mV/dec ($2 \times 2.303RT/F$) or higher is generally observed.[22] Similarly, a Tafel slope of ∼29 mV/dec ($2.303RT/2F$) is an indication of a rate-determining Tafel reaction, and a Tafel slope of ∼39 mV/dec ($2 \times 2.303RT/3F$) is an indication of a rate-determining Heyrovsky reaction.[22] Since all Tafel slopes observed for the MoS_2 films and nanocube structures were higher than 118 mV/dec, this means that the formation of atomic H is most likely the rate-determining reaction step. The large deviation from the theoretical value may be due to the Au substrate having a low conductivity, or to a too high uncompensated resistance in

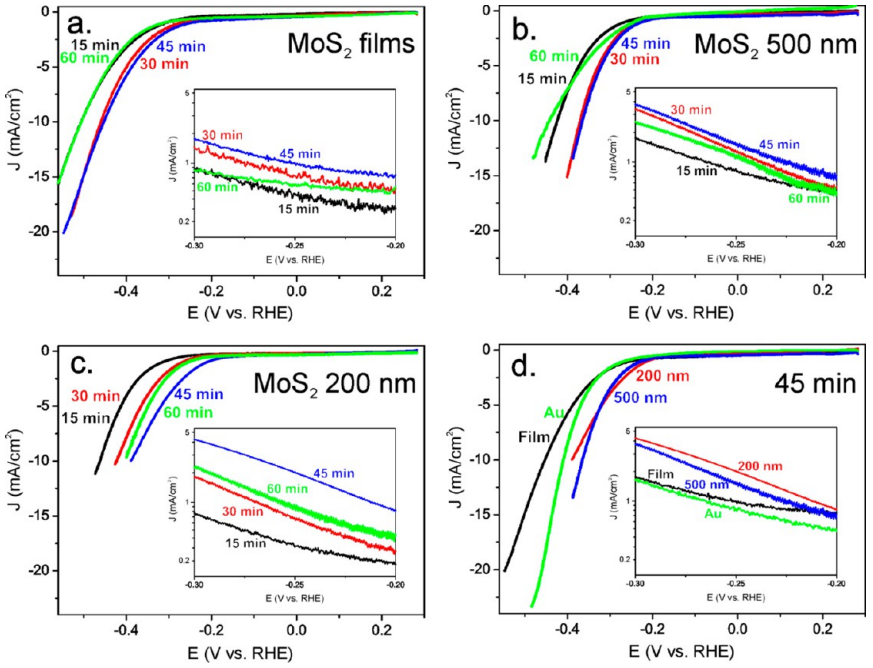

Figure 6. LSV measurements and corresponding Tafel plots (insets) of (a) MoS_2 films after MoS_2 deposition for 15 min (black line), 30 min (red line), 45 min (blue line), and 60 min (green line); (b) 500 nm MoS_2 nanocube structures after MoS_2 deposition for 15 min (black line), 30 min (red line), 45 min (blue line), and 60 min (green line); (c) 200 nm MoS_2 nanocube structures after MoS_2 deposition for 15 min (black line), 30 min (red line), 45 min (blue line), and 60 min (green line); (d) comparison between Au film (green line) and several MoS_2 architectures after 45 min of MoS_2 deposition on a film (black line), on 500 nm nanocubes (blue line) and on 200 nm nanocubes (red line). All LSV curves were measured in negative direction from 0.28 to −0.59 V vs RHE using a step potential of −0.3 mV and a scan rate of 5 mV/s in an electrolyte containing H_2SO_4 at pH 0.24, which was stirred during LSV measurements and had been purged with N_2 prior to the measurements. The presented current densities were calculated for the real surface area. Because the current was found to be limited by the counter electrode for high overpotentials, the shown curves were cut off before a plateau was observed.

Table 1. Overview of Overpotentials Needed to Reach a Current Density of −1 and −5 mA/cm^2, Tafel Slopes and Exchange Current Densities for Different Samples Used in This Study, Including a Comparison with Literature Data

sample	overpotential needed for −1 mA/cm^2 (mV)	overpotential needed for −5 mA/cm^2 (mV)	Tafel slope (mV/dec)	exchange current density J_0 (mA/cm^2)
film 15 min	310	438	180	2.0×10^{-2}
film 30 min	270	400	179	2.9×10^{-2}
film 45 min	250	387	189	4.4×10^{-2}
film 60 min	310	442	179	1.7×10^{-2}
500 nm 15 min	260	373	154	1.9×10^{-2}
500 nm 30 min	240	328	131	1.6×10^{-2}
500 nm 45 min	230	321	134	2.0×10^{-2}
500 nm 60 min	240	365	141	1.9×10^{-2}
200 nm 15 min	320	414	142	6.1×10^{-3}
200 nm 30 min	270	366	128	7.8×10^{-3}
200 nm 45 min	210	320	141	3.2×10^{-2}
200 nm 60 min	260	350	132	1.2×10^{-2}
Au film	260	370	135	9.4×10^{-3}
MoS_2 nanopolygons[17]	100 (onset)	n.a.	55−60	$1.3–3.1 \times 10^{-4}$
amorphous Co-MoS_3[22]	140	175	40	1.3×10^{-4}
amorphous MoS_3[5]	170	n.a.	43	5.0×10^{-4}
MoO_3−MoS_2 nanowires[4]	207	264	50−60	n.a.
double-gyroid MoS_2[19]	300	n.a.	n.a.	n.a.
vertically aligned MoS_2[18]	330	370	105−120	2.2×10^{-3}

our setup.[4] Unfortunately, a large variation in *iR* drop (25−75 Ω) was observed when we used impedance or I-interrupt techniques for measurement of the uncompensated resistance. Consequently, attempts for *iR*-correction failed, because similar *iR* drops were expected for different samples. Since false *iR*-correction may add inappropriate distortions to the original data, it was decided to present the data without *iR*-correction. As the nanocubes show a smaller average Tafel slope than the

planar films, the nature of the active sites may be distinctively different, which can be explained by the availability of more catalytically active edge sites on the nanocube samples. As expected from the LSV curves, J_0 is the highest after a deposition time of 45 min for all MoS_2 structures compared in this study.

The bottom part of Table 1 provides an overview of the characteristics of a few of the best MoS_2 systems reported in literature.[4,5,17−19,22] It is noted that all measurements (this study and the comparison with literature) were performed in acidic solutions with pH between 0.0 and 0.5. Considering the overpotential needed to reach a current density of −1 mA/cm^2, the MoS_2 nanocube structures as presented in this study are comparable to the performances of the literature systems, having an early onset potential and therefore a relatively low overpotential at a current density of −1.0 mA/cm^2. Only MoS_2 nanopolygons with a very high concentration of edge sites and amorphous MoS_3 films with or without Co promotion show an earlier onset potential,[5,17,22] and the required overpotential for our system is approximately the same as that for MoO_3−MoS_2 nanowires.[4] Since the amorphous MoS_3 films were also prepared by electrodeposition, it is expected that applying the exact same synthesis procedure using Co promotion on top of the nanocube structures from this study might improve the H_2 evolution activity even further. It is noted that we obtained very high Tafel slopes compared to the values as reported in most literature, which also resulted in a relatively larger overpotential needed to reach a current density of −5 mA/cm^2. The Tafel slopes reported in literature (40−60 mV/dec) indicate a rate-determining desorption step via an ion+atom reaction (Heyrovsky step),[4,5,17,22] whereas the nanocubes in our study showed a rate-determining H formation reaction (Volmer step). A possible explanation for the shift in reaction mechanism may be the fact that our MoS_2 samples are composed of many nanosized domains. Consequently, a high concentration of defect sites, as observed from the TEM image in Figure 5, may have led to different predominant mechanisms than the regular catalytic centers at the edge sites.

It is envisaged that MoS_2 could be employed as a segment in photocatalytic nanowires or nanocubes made via templated electrodeposition for improved H_2 formation.[30] Since electrodeposition yields MoS_2 with a preferred orientation of the MoS_2 layers parallel to the substrate as observed here, it is expected that a high density of edge sites would be located at the template wall. In this way, a high density of edge sites would be exposed at the nanowire surface upon template removal, which would increase the H_2 evolution rate.

To illustrate the versatility of the presented technique for the synthesis of nanocube structures of arbitrary composition, also Pt was deposited on top of PMMA−Au nanocube structures. As shown in Figure 7a,b, these Pt nanocube structures have the same polycrystalline morphology as observed elsewhere.[31] As shown in Figure 1, the same procedure for NIL and sidewall deposition can also be applied for the synthesis of Au nanobox structures instead of PMMA−Au nanocube structures. These nanobox structures can also be coated with an arbitrary second material via electrodeposition as shown in Figure 7c for the case of Ni. In this figure, the false color difference between the Au template (gray) and electrodeposited Ni (white) indicates the location of the two phases, and EDX mapping (not shown) also confirmed deposited Ni at the outside of the Au nanoboxes. Incomplete PMMA removal may be the reason that no Ni deposition was observed at the inside of the Au nanoboxes. A closer look at the Au−Ni nanobox structures shows that the corners of the Au phase are sharper than that of the Ni phase due to the previously described "blanketing" effect.

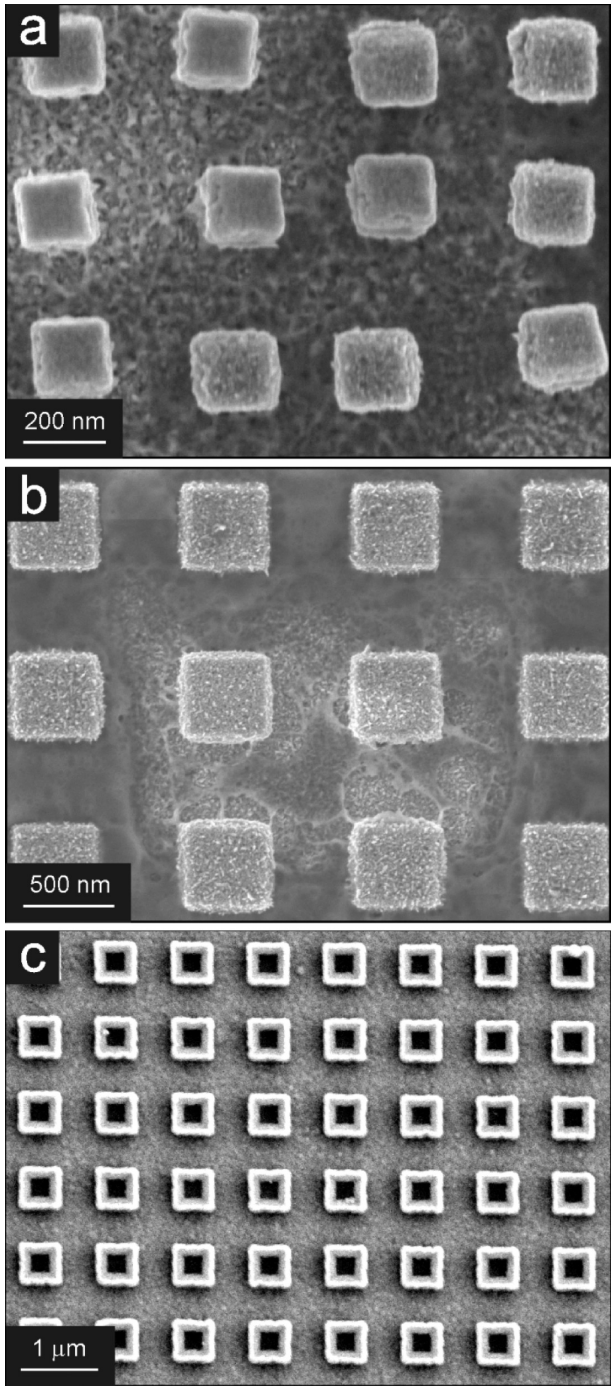

Figure 7. (a) Pt nanocube structures with a lateral size of ∼200 nm, (b) Pt nanocube structures with a lateral size of ∼500 nm, and (c) open Ni nanobox structures with a lateral size of ∼500 nm.

CONCLUSIONS

Au nanocube structures made by a combination of nanoimprint lithography (NIL) and sidewall deposition were conformally covered with a desired material using electrodeposition. After deposition of MoS_2 on top of these Au nanocube structures, the activity toward the H_2 evolution reaction (HER) was significantly increased compared to MoS_2 films, because a

higher relative density of catalytically active MoS_2 edge sites was available on these nanocubes. Rounding of the corners of MoS_2 nanocube structures is probably responsible for a decrease in HER activity after longer deposition times, since it is energetically more favorable for the system to minimize its total surface area, thereby exposing fewer edge sites. Therefore, MoS_2 nanocube structures with a ~30 nm thick MoS_2 layer were found to be most active in H_2 evolution. These Au nanocube structures can also be used for the synthesis of nanocubes composed of other materials like Pt and Ni.

AUTHOR INFORMATION

Corresponding Author

*E-mail: j.e.tenelshof@utwente.nl. Tel: +31 (0)53 489 2695.

Present Address

[‖]M.R. and K.-S.C.: University of Wisconsin—Madison, 1101 University Avenue, Madison, WI 53706, USA.

Notes

The authors declare no competing financial interest.

ACKNOWLEDGMENTS

Financial support from the Chemical Sciences division of The Netherlands Organization for Scientific Research (NWO-CW) in the framework of the TOP program, and from the Fulbright Center in The Netherlands, is gratefully acknowledged. Financial Support from the Division of Chemical Sciences, Geosciences, and Biosciences, Office of Basic Energy Sciences of the U.S. Department of Energy through Grant DE-FG02-05ER15752 is also gratefully acknowledged by K.-S.C. and M.R..

REFERENCES

(1) Bak, T.; Nowotny, J.; Rekas, M.; Sorrell, C. C. *Int. J. Hydrogen Energy* **2002**, *27*, 991−1022.

(2) Kudo, A.; Miseki, Y. *Chem. Soc. Rev.* **2009**, *38*, 253−278.

(3) Maeda, K. *J. Photochem. Photobiol., C* **2011**, *12*, 237−268.

(4) Chen, Z.; Cummins, D.; Reinecke, B. N.; Clark, E.; Sunkara, M. K.; Jaramillo, T. F. *Nano Lett.* **2011**, *11*, 4168−4175.

(5) Merki, D.; Fierro, S.; Vrubel, H.; Hu, X. *Chem. Sci.* **2011**, *2*, 1262−1267.

(6) Min, S.; Lu, G. *J. Phys. Chem. C* **2012**, *116*, 25415−25424.

(7) Sobczynski, A. *J. Catal.* **1991**, *131*, 156−166.

(8) de Beer, V. H. J.; Dahlmans, J. G. J.; Smeets, J. G. M. *J. Catal.* **1976**, *42*, 467−470.

(9) Farag, H.; Sakanishi, K.; Kouzu, M.; Matsumura, A.; Sugimoto, Y.; Saito, I. *J. Mol. Catal. A: Chem.* **2003**, *206*, 399−408.

(10) Sun, Y.; Wang, H.; Prins, R. *Catal. Today* **2010**, *150*, 213−217.

(11) Efeoglu, I.; Baran, Ö.; Yetim, F.; Altintaş, S. *Surf. Coat. Technol.* **2008**, *203*, 766−770.

(12) Fleischauer, P. D.; Lince, J. R. *Tribol. Int.* **1999**, *32*, 627−636.

(13) Xing, Y.; Deng, J.; Wu, Z.; Lian, Y. *Appl. Mech. Mater.* **2012**, *229−231*, 35−39.

(14) Pourabbas, B.; Jamshidi, B. *Chem. Eng. J.* **2008**, *138*, 55−62.

(15) Raybaud, P.; Hafner, J.; Kresse, G.; Kasztelan, S.; Toulhoat, H. *J. Catal.* **2000**, *189*, 129.

(16) Seivane, L. F.; Barron, H.; Botti, S.; Marques, M. A. L.; Rubio, Á.; López-Lozano, X. *J. Mater. Res.* **2013**, *28*, 240−249.

(17) Jaramillo, T. F.; Jørgensen, K. P.; Bonde, J.; Nielsen, J. H.; Horch, S.; Chorkendorff, I. *Science* **2007**, *317*, 100−102.

(18) Kong, D.; Wang, H.; Cha, J. J.; Pasta, M.; Koski, K. J.; Yao, J.; Cui, Y. *Nano Lett.* **2013**, *13*, 1341−1347.

(19) Chen, Z.; Kibsgaard, J.; Jaramillo, T. F. *Proc. SPIE* **2010**, DOI: 10.1117/12.860659.

(20) Bonde, J.; Moses, P. G.; Jaramillo, T. F.; Nørskov, J. K.; Chorkendorff, I. *Faraday Discuss.* **2008**, *140*, 219−231.

(21) Hinnemann, B.; Moses, P. G.; Bonde, J.; Jørgensen, K. P.; Nielsen, J. H.; Horch, S.; Chorkendorff, I.; Nørskov, J. K. *J. Am. Chem. Soc.* **2005**, *127*, 5308−5309.

(22) Merki, D.; Vrubel, H.; Rovelli, L.; Fierro, S.; Hu, X. *Chem. Sci.* **2012**, *3*, 2515−2525.

(23) Nguyen, M.; Tran, P. D.; Pramana, S. S.; Lee, R. L.; Batabyal, S. K.; Mathews, N.; Wong, L. H.; Graetzel, M. *Nanoscale* **2013**, *5*, 1479−1482.

(24) Chou, S. Y.; Krauss, P. R.; Zhang, W.; Guo, L.; Zhuang, L. *J. Vac. Sci. Technol. B* **1997**, *15*, 2897−2904.

(25) Austin, M. D.; Ge, H.; Wu, W.; Li, M.; Yu, Z.; Wasserman, D.; Lyon, S. A.; Chou, S. Y. *Appl. Phys. Lettt.* **2004**, *84*, 5299−5301.

(26) Cha, N. G.; Kanki, T.; Tanaka, H. *Nanotechnology* **2011**, 22.

(27) Cha, N. G.; Lee, B. K.; Kanki, T.; Lee, H. Y.; Kawai, T.; Tanaka, H. *Nanotechnology* **2009**, 20.

(28) Hattori, A. N.; Ono, A.; Tanaka, H. *Nanotechnology* **2011**, 22.

(29) Hendricks, T. R.; Lee, I. *Nano Lett.* **2007**, *7*, 372−379.

(30) Maijenburg, A. W.; Rodijk, E. J. B.; Maas, M. G.; Enculescu, M.; Blank, D. H. A.; Ten Elshof, J. E. *Small* **2011**, *7*, 2709−2713.

(31) Maijenburg, A. W.; George, A.; Samal, D.; Nijland, M.; Besselink, R.; Kuiper, B.; Kleibeuker, J. E.; Ten Elshof, J. E. *Electrochim. Acta* **2012**, *81*, 123−128.